Influence of afterbody rounding on the near wake of fastback vehicle

Giacomo Rossitto, Christophe Sicot, Valérie Ferrand, Jacques Borée, Fabien Harambat

Influence of afterbody rounding on the near wake of fastback vehicle

G.Rossitto[1,2,*], C. Sicot[2], V. Ferrand[3], J. Borée[2] and F. Harambat[1]

1: PSA Groupe, Velizy-Villacoublay, France.
2: Institut Pprime, UPR-3346 CNRS, ENSMA, Université de Poitiers, France
3: Institut Supérieur de l'Aéronautique et de l'Espace (ISAE-SUPAERO), Université de Toulouse, France.
*Correspondent author: giacomo.rossitto@ensma.fr

Keywords: PIV, Drag Reduction, Wake analysis, Vorticity, Rounded edges

ABSTRACT

Experimental and numerical analyzes were performed to investigate the aerodynamic performances of a realistic vehicle with different afterbody rounding. Rounding the side pillars generated moderate changes in drag and important lift reductions. The minor effect on the drag force was found to result from opposite drag effects on the slanted and vertical surfaces. The vorticity distribution in the near wake was also analyzed to understand the flow field modifications due to afterbody rounding.

1. Introduction

For the last decades car manufacturers have been facing the challenging task of reducing fuel consumption and CO_2 emissions. In response to that, optimization algorithms have been applied to generate new vehicle shapes minimizing the aerodynamic drag. Since the obtained optimum shapes has no brand differentiating details, stylists are nowadays trying to give back a brand signature by proposing "non-conventional" shapes. In that framework, important rear pillars rounding becomes a differentiation strategy. The current study suggests to qualify the influence of such afterbody rounding on the flow field and on drag development over a fastback vehicle.

Very few papers have addressed the question of rear edges curvature in aerodynamic vehicle performances. One of the first works was presented by Gilhaus et al. [1] and Howell [2]. Thanks to balance measurements, it was found that rounded pillars reduced drag and rear lift but yawing moment had a pronounced increase. Only recently, advanced techniques were used to achieve better understanding of the afterbody rounding. Thacker et al. [3] showed that rounding the edge between the roof and the rear slant of the Ahmed body results in a 10% drag reduction. Authors attributed this reduction to the fully attached flow over the backlight and the downstream shift of the rotating structures developing in the near wake. Fuller et al. [4] analyzed the benefits of rounding the rear side pillars on the Davis model. They observed that rounded edges generate a different wake structure dominated by the interaction between the longitudinal vortices and the separated region. The rounded edges model resulted in drag and lift reduction of 11% and 25%

respectively. The impact of afterbody rounding was mentioned also during the development of the Tesla Model S by Palin et al. [5]. Important curved side pillars were avoided to reduce highly dynamic wake, which caused large variation in base pressure.

From the literature review, it appears that rounding afterbodies affects considerably aerodynamic loads and flow development, but systematic investigation into the effects of changing radii of side backlight edges was not reported. In complement to the recent study proposed by the same authors in [6] over a simplified car model (Ahmed body), the present study addresses this question on a realistic car model equipped with various rear pillars curvatures. Special care is taken to understand how the modified flow on the backlight interacts with the near wake and promotes drag and lift changes.

Four rear ends were analyzed combining PIV to balance and wall pressure measurements to fully characterize the flow structures and the associated aerodynamic forces. Complementary numerical simulations were systematically applied to complete the experimental data and help physical analysis.

1.1. Experimental and numerical set-up

The model and its relevant dimensions are reported in *figure 1.* Four rear ends are tested, they differ by their side pillars curvature. The curvature radius is given as a percentage of the model span, i.e. 300mm. The model equipped with sharp pillars having 0% radius is referred as S_0 and it is considered as the reference case. The others models are S_8, S_{20} and S_{40}. All the rear ends have the same curvature at the end of the roof to avoid flow separation. The corresponding radius is chosen to maximize the room for the rear passengers for a fixed backlight angle of 23 degrees. The horizontal projection of the slanted surface, $\xi, = 440mm$, will be used as reference length. Starred spatial coordinates are normalized by the reference length.

The experimental results reported in this work were obtained from tests conducted in the PSA Groupe wind tunnel of La Ferté Vidame. The Eiffel wind tunnel is 52 meters long and has a test section 2 meters high, 5.2 meters large and 6 meters long. It has a maximum free stream velocity of 53 m/s. The wind tunnel blockage ratio was 1.4%. All the data were obtained at 40m/s which gives a Reynolds number based on the length of the model of 2.6**e**6. Starred velocities are normalized by the free stream velocity. A six components balance was used to measure the aerodynamic forces acting on the model. The drag and lift coefficients were calculated as follows:

$$C_{d,l} = \frac{F_{d,l}}{\frac{1}{2}\rho U_0^2 S}$$

where F is the force measured by the balance, ρ the density of the air, and S the frontal surface area

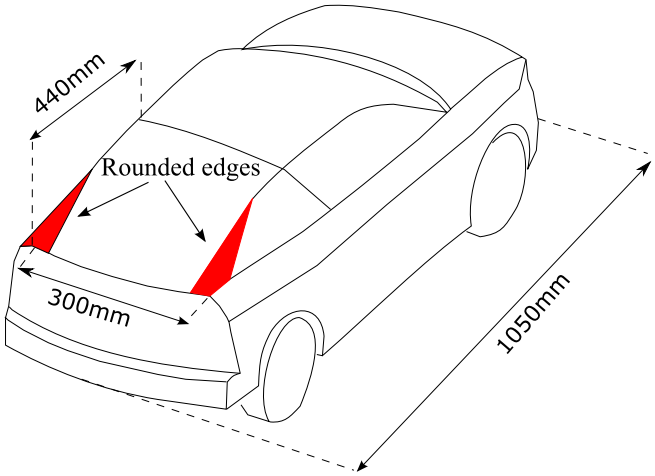

Figure 1: Fastback vehicle model and location of the rounded edges

of the model. The precision of the balance was 0.001 for the drag coefficient Cd and 0.002 for the lift coefficient Cl.

Static wall pressure was recorded by 35 pressure probes over the vertical surface of the rear end. Those probes were connected to a SCANdaq 8000 acquisition system. The acquisition rate was 40 Hz for 3000 samples giving 75s of time recording. The static wall pressure coefficient at one point i was computed from the expression:

$$C_P(i) = \frac{P(i) - P_0}{\frac{1}{2}\rho U_0^2}$$

where $P(i)$ is the static pressure of point (i), P_0 the static pressure measured upstream of the model. The static accuracy of the system is $\pm$13Pa, i.e. 0.015 Cp.

Furthermore, PIV measurements were performed in the wake of the model. The laser sheet was set by a 2*120mJ Nd:Yag Quantum Big Sky Laser. The Dantec Flowsense 4M mkII camera (2024pixel*2024 pixels) equipped with 105 mm lenses generated 462mm*462mm fields of view. 2D PIV was performed on the symmetry (x,z) plane Y^*=0. Cross-flow planes (y,z), were recorded using the Stereo-PIV technique to obtain the 3 velocity components of the flow field. For all the PIV measurements, post-processing was performed with a final interrogation window of 16*16 pixels, after an initial window of 32*32 pixels, with an overlap of 50% in horizontal and vertical directions. The grid spacing was 1.82mm. A SNR filter was applied to remove vectors with SNR$<$ 1.2. 900 images were recorded with a 7Hz trigger rate. With this setting, the 95% confidence limit represents approximately $\pm$3% of the mean velocity [7].

The numerical simulations presented in this work were computed with the commercial code PowerFLOW© (version 5.0c) based on lattice Boltzmann model. The simulation setting is reported

in *table 1.* The model size for the numerical simulations corresponds to a real vehicle scale. At Reynolds 1.04**e**7, 324000 time-steps were computed (3 seconds of real time). Local variable refinement regions VRs were defined to locally allow coarsening the grid by a factor of 2 starting from the *Minimum Level of VR* [8]. The computational grid consisted of 1.2 million volume elements and 0.6 million surface elements. In the following, temporally averaged velocity and pressure fields will be shown. These averages are computed over approximately 25 convective time scales L/U_0 where L is the length of the body and U_0 the external velocity.
This setting allowed good agreements between numerical and experimental results, as it is possible to examine in *figure 1.1* that reports a comparison of mean streamwise velocity profiles.

Physical Time Scaling	1 timestep $= 9.308e-06sec$
Minimum Level of VR	VR 9 (2.50e-03 m/voxel)
Simulation time	324000 timesteps (3 sec)
Reynolds	1.04402e+07

Table 1: Numerical PowerFLOW© setting

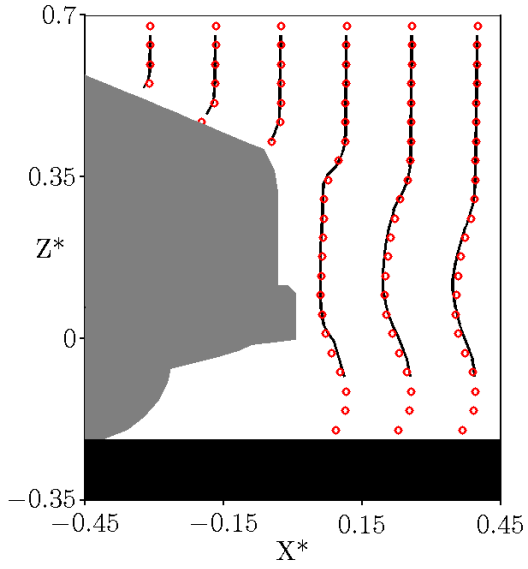

Figure 2: Comparison of mean streamwise velocity profiles. ○ Numerical, – Experimental

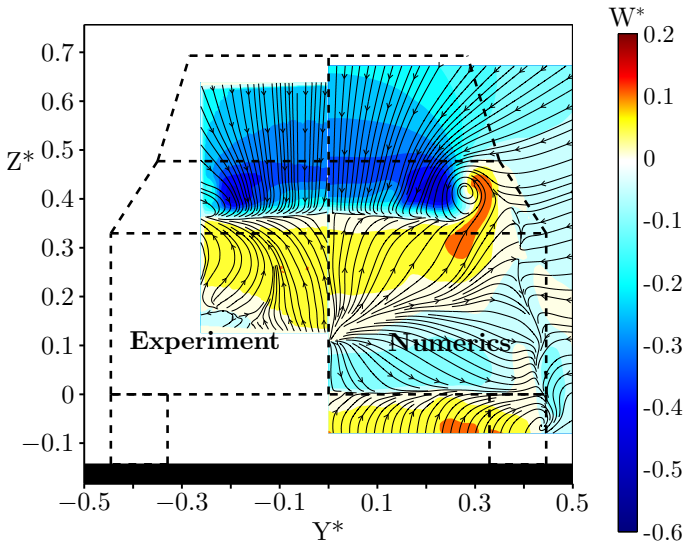

Figure 3: Comparison of mean normal velocity W^*. Plane at X * =0.02. The dashed lines represent the geometry of the model

2. Base Geometry flow analysis

Table 2 reports the variation of aerodynamic coefficients and averaged base pressure with respect to the reference case S_0. Increasing the side radius generates a small drag reduction and significant lift reduction. For the S_0 configuration, most of the rear lift is generated over the rear end

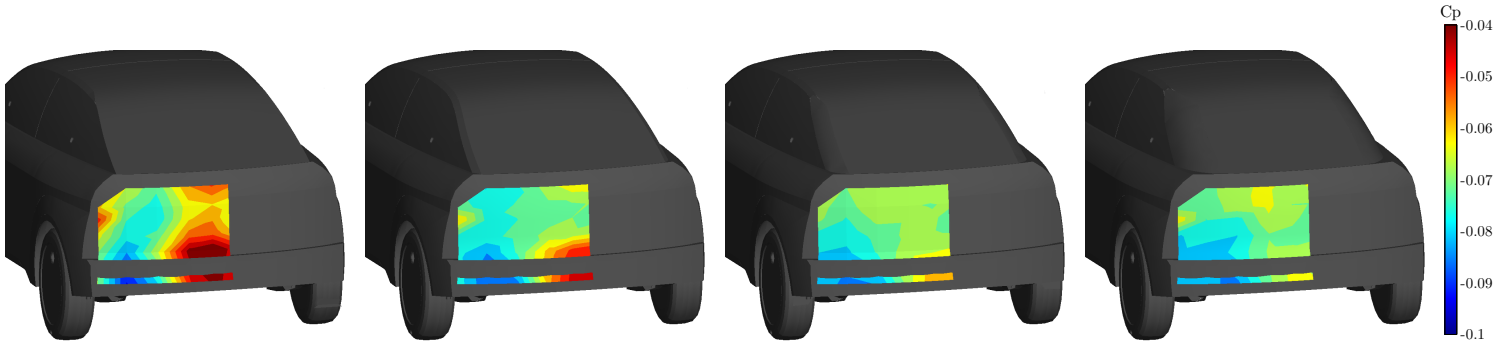

(a) S_0 (b) S_8 (c) S_{20} (d) S_{40}

Figure 4: Experimental wall pressure coefficient distribution over the vehicle base.

by the low value of pressure over the curved roof edge and from the low pressure foot-print of the longitudinal vortices, the so-called C-pillar vortices [6]. These vortices are generated by the interaction of the flow coming from the side of the model and the flow over the rear window. Since the roof radius is constant among the four models, lift reductions are caused by the C-pillar vortices intensity modifications due to side rounding. For a moderate value of C-pillars rounding, the origin of the longitudinal vortices is displaced towards the base of the body along the C-pillars [6]. For larger rounding, three-dimensional flow separation does not occur anymore on the side of the model and thus the side vortices disappear [9]. The weakening of the C-pillar vortices allows a pressure recovery over the rear window reducing its contribution to drag and lift. However, the variation of the average base pressure over the vertical surface, reported in *figure 4* and in *table 2*, gives evidence that the base pressure is reduced when the curvature side radius is increased. For S_{40}, the base pressure is 17% lower than for S_0, resulting in an important local drag increase. This effect counter-balances the local drag reduction of the rear window and can explain the weak effect of pillars rounding on the global drag (*table 2*).

	ΔCd	ΔCl	ΔCp Base
S_0	-	-	-
S_8	0%	-13%	-12%
S_{20}	-1.5%	-18%	-15%
S_{40}	-2%	-27%	-17%

Table 2: Variation of aerodynamic coefficients and averaged base pressure compared to S_0.

The mean velocity fields in the symmetry plane are reported in *figure 5*. It was chosen not to report the intermediate configurations, i.e. S_8 and S_{20}, to focus on the main differences between the most rounded rear pillar model S_{40} and the sharpest one S_0. The symmetry plane is far from sufficient to describe the entire topology of the tridimensional near wake, nevertheless it is very useful to get a first hint of the changes made by side rounding. Over the rear window, no major differences are

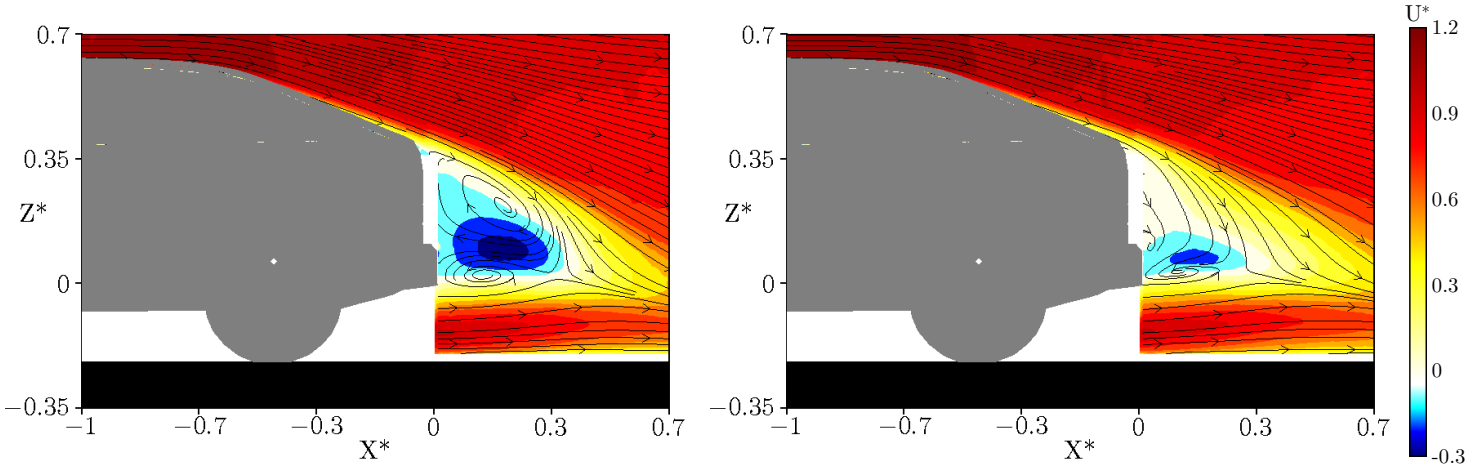

(a) S_0 (b) S_{40}

Figure 5: Time averaged streamlines and mean streamwise velocity U^* at Y^*=0.

noticed between the two models. The flow is attached to the slanted surface due to the important roof radius for both models. For S_0, the average separated zone in the close wake is characterized by two counter-rotating structures. The mean recirculating length, identified by the saddle point of the 2D mean streamlines, is at X^*= 0.33 and X^*= 0.23 respectively for S_0 and S_{40}. Adding pillar curvature reduces then the length of the near wake and modifies the topology of the enclosed structures. For S_{40}, the mean curvature of the near wake is increased due to important negative normal velocity. Regarding the flow organization inside the near wake, the upper structure is not evidenced anymore and the lower structure seems to be reduced. Such a strong modification of the near wake properties in the symmetry plane, may result from a 3D modification of the flow field due to side rounding.

To understand this complex mechanism, cross-flow planes are displayed in *figures 6 and 7*. The data are issued from the numerical simulations to overcome the size limitation of the experimental data. Each picture is divided in two: the left side represents S_0 and the right side S_{40}. At X^*= 0.02, right after the rear slant, the longitudinal vorticity ($\Omega_x{}^* = \frac{\Omega_{x*}\xi}{U_0}$) is concentrated in the C-pillar vortex for S_0 (*figure 6*). At the same X plane, a diffuse horizontal small area of longitudinal vorticity is present for S_{40} located in the shear layer (*figure 6*). Two-dimensional lines tangent at each point to the vector (V,W) are also drawn in *figure 6* to underline the different organization of flow fields due to afterbody rounding. At X^*= 0.23, i.e. the S_{40} saddle point location, the overall longitudinal rotation of the S_{40} near wake is showed in *figure 7*. The high spanwise and vertical velocity associated to the transversal flow in S_{40}, therefore results in a global longitudinal rotation of the flow in the near wake.

To quantify the rotation of the flow, the longitudinal evolution of the mean circulation $\Gamma^* = \int_{S^*} \Omega_x^* dS$, reported in *figure 8*, was analyzed as in the work of Rossitto et al. [6]. The domain of the calculation included all the numerical domain presented in *figure 6*. In the near wake, i.e. $X^* \in [0; 0.4]$,

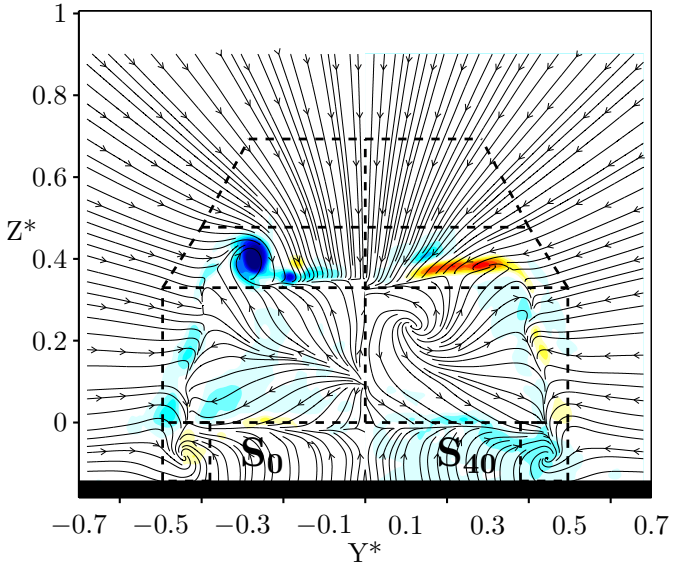

Figure 6: Mean Streamwise Vorticity Ω^*_x at X^*= 0.02. Left S_0, Right S_{40}.

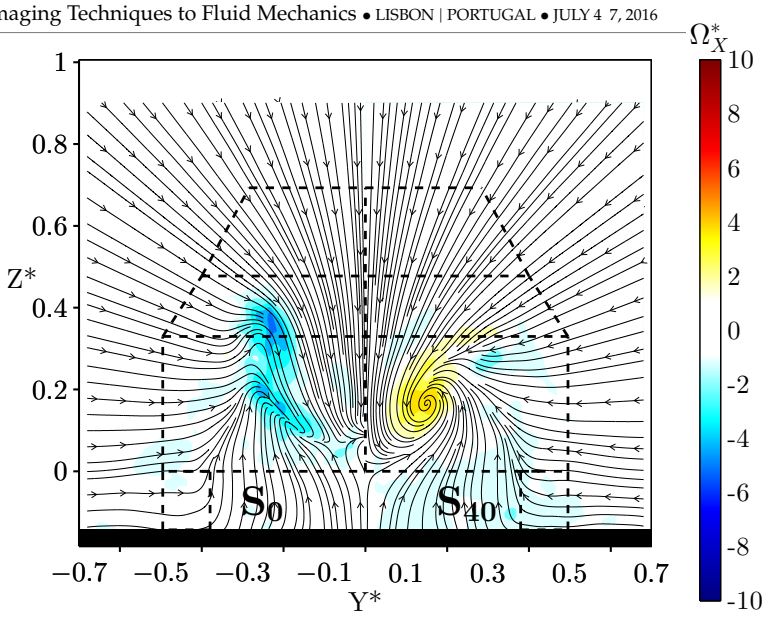

Figure 7: Mean Streamwise Vorticity Ω^*_x at X^*= 0.23. Left S_0, Right S_{40}.

the mean recirculation is higher in for S_0 respect to S_{40}. In fact, despite the high levels of vorticity of the C-pillar vortices for S_0 , at X^*= 0.02, Γ^* for S_{40} is 20% higher than S_0. The flow overcoming the rounded edge results then in a notably 3D organization characterized by a large scale rotation around the longitudinal axis. The longitudinal rotation, as reported in *figure 9*, generates a lower pressure for S_{40} respect to S_0, consistently with the pressure wall measurements analyzed previously in *figure 4* related to the local base drag increase.

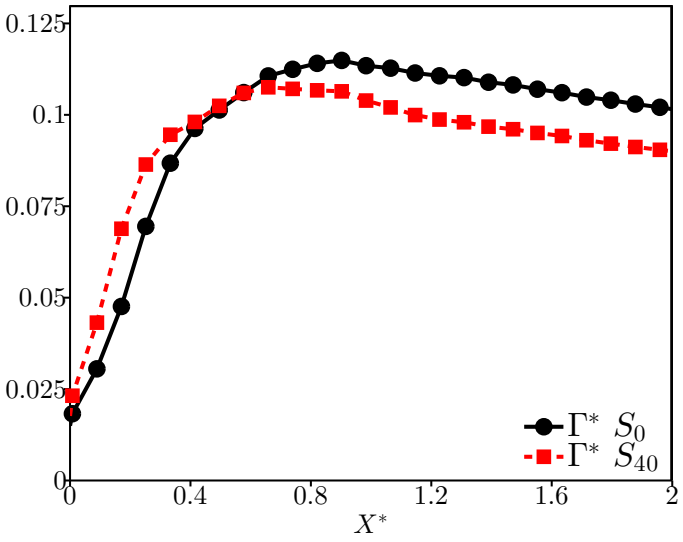

Figure 8: Longitudinal evolution of the mean circulation

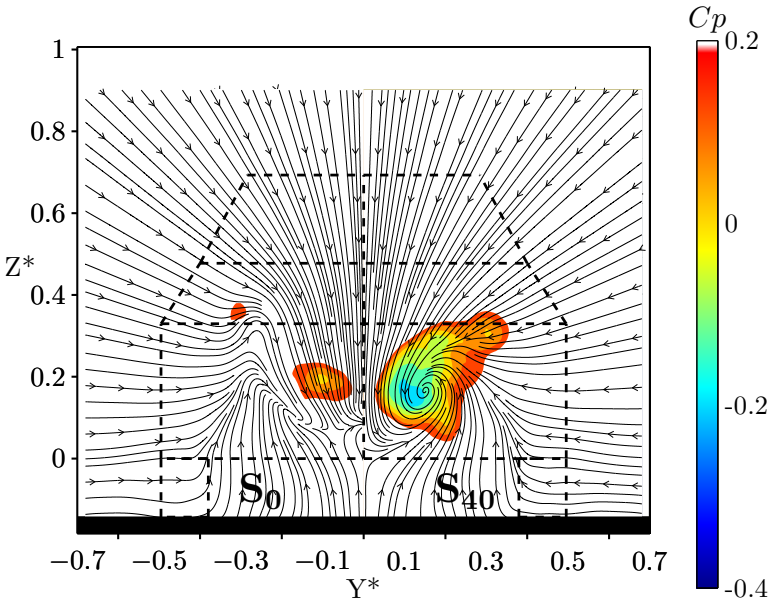

Figure 9: Mean pressure coefficient Cp at X^*= 0.23. Left S_0, Right S_{40}.

After $X^* = 0.4$, Γ^* is higher for the sharp model than for the rounded one, in accord with the lift value reported in *Table 2*. *Figure 10* reports the time averaged streamlines issued from the numerical simulations. A comparison between the two models permits to reveal the mean differences generated by side pillars rounding. The sharp side pillars force the lateral flow to separate, generating longitudinal vortices. As analyzed by the same authors in [6], it is suggested that, for S_0, the sharp lateral edges "shield" the wake separation region at the base and enable a "two-dimensional" separation,"2D" meaning that the mean streamlines at separation are more parallel to the orientation of the flow over the window, while longitudinal vorticity is concentrated in the C-pillar vortices. On the contrary, for rounded edges, the flow is drawn in from the sides, toward the center over the slanted surface. The separation at the base is then notably 3D for S_{40}, associated with high spanwise and vertical velocity components [6].

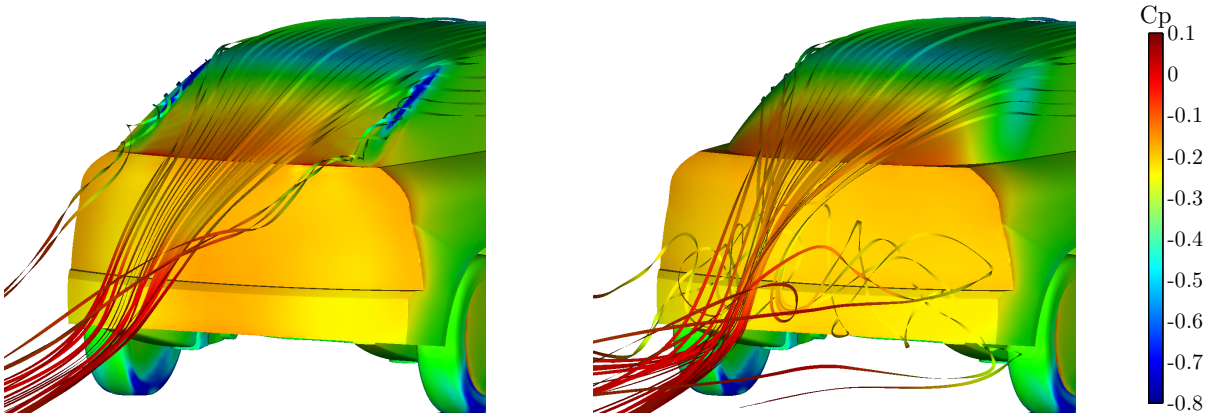

(a) S_0 (b) S_{40}

Figure 10: Time averaged streamlines from numerical simulations. The streamlines and the surface of the body are colored by the pressure coefficient C_p

3. Conclusions

Experimental and numerical analyzes were used to study the influence of afterbody rounding on the aerodynamic characteristics of a fastback vehicle model. Rounded edges resulted having minimal impact on drag due to opposite effects over the rear slant and the base. Important lift reductions were achieved thanks to the elimination of the C-pillar vortices. The impact of rounded edges on the near wake organization due to the different longitudinal vorticity distribution was highlighted.

This work has been performed in the framework of the "OpenLab Fluidics" @Poitiers.

References

[1] Alfons M Gilhaus and Volker E Renn. Drag and driving-stability-related aerodynamic forces and their interdependence-results of measurements on 3/8-scale basic car shapes. Technical report, SAE Technical Paper, 1986.

[2] JP Howell. C466/036 shape features which influence crosswind sensitivity. 9(1):43–43, 1993.

[3] Adrien Thacker, S Aubrun, A Leroy, and Philippe Devinant. Effects of suppressing the 3d separation on the rear slant on the flow structures around an ahmed body. *Journal of Wind Engineering and Industrial Aerodynamics*, 107:237–243, 2012.

[4] Joshua Fuller and Martin A Passmore. The importance of rear pillar geometry on fastback wake structures. *Journal of Wind Engineering and Industrial Aerodynamics*, 125:111–120, 2014.

[5] Robert Palin, Vincent Johnston, Shaun Johnson, Andrew D'Hooge, Bradley Duncan, and Joaquin Ivan Gargoloff. The aerodynamic development of the tesla model s-part 1: Overview. Technical report, SAE Technical Paper, 2012.

[6] Giacomo Rossitto, Christophe Sicot, Valérie Ferrand, Jacques Borée, and Fabien Harambat. Influence of afterbody rounding on the pressure distribution over a fastback vehicle. *Experiments in Fluids*, 57(3):1–12, 2016.

[7] LH Benedict and RD Gould. Towards better uncertainty estimates for turbulence statistics. *Experiments in fluids*, 22(2):129–136, 1996.

[8] Ehab Fares. Unsteady flow simulation of the ahmed reference body using a lattice boltzmann approach. *Computers & fluids*, 35(8):940–950, 2006.

[9] G. Rossitto, C. Sicot, V. Ferrand, J. Borée, and F. Harambat. Wake structure and drag of vehicles with rounded rear edges. In *50th International Conference on Applied Aerodynamics. 3AF*, 2015.